PCCP

PAPER

View Article Online
View Journal | View Issue

Cite this: *Phys. Chem. Chem. Phys.*, 2014, **16**, 12299

Sol-flame synthesis of cobalt-doped TiO_2 nanowires with enhanced electrocatalytic activity for oxygen evolution reaction†

Lili Cai,[a] In Sun Cho,[a] Manca Logar,[ab] Apurva Mehta,[c] Jiajun He,[d] Chi Hwan Lee,[a] Pratap M. Rao,[a] Yunzhe Feng,[e] Jennifer Wilcox,[d] Fritz B. Prinz[a] and Xiaolin Zheng*[a]

Received 23rd April 2014,
Accepted 1st May 2014

DOI: 10.1039/c4cp01748j

www.rsc.org/pccp

Doping nanowires (NWs) is of crucial importance for a range of applications due to the unique properties arising from both impurities' incorporation and nanoscale dimensions. However, existing doping methods face the challenge of simultaneous control over the morphology, crystallinity, dopant distribution and concentration at the nanometer scale. Here, we present a controllable and reliable method, which combines versatile solution phase chemistry and rapid flame annealing process (sol-flame), to dope TiO_2 NWs with cobalt (Co). The sol-flame doping method not only preserves the morphology and crystallinity of the TiO_2 NWs, but also allows fine control over the Co dopant profile by varying the concentration of Co precursor solution. Characterizations of the TiO_2:Co NWs show that Co dopants exhibit 2+ oxidation state and substitutionally occupy Ti sites in the TiO_2 lattice. The Co dopant concentration significantly affects the oxygen evolution reaction (OER) activity of TiO_2:Co NWs, and the TiO_2:Co NWs with 12 at% of Co on the surface show the highest OER activity with a 0.76 V reduction of the overpotential with respect to undoped TiO_2 NWs. This enhancement of OER activity for TiO_2:Co NWs is attributed to both improved surface charge transfer kinetics and increased bulk conductivity.

Introduction

Doping, or intentional incorporation of impurities, is a fundamental method to modify the electronic,[1–3] chemical,[4,5] optical[6,7] and magnetic[8–10] properties of host materials. Doping materials has impacted a range of applications, such as solar cells, transistors, integrated circuits, photocatalysis, bioimaging, light-emitting diodes and spintronics. Doping nanowires (NWs) can lead to unique properties arising from their nanoscale dimensions,[11–14] but it faces the challenge of simultaneous control over the morphology, crystallinity, dopant distribution and concentration at the nanometer scale. Existing doping methods for nanostructured materials can be broadly categorized into *in situ* and *ex situ* methods. *In situ* doping methods incorporate dopants during the material growth by methods such as solid-state mixing,[15,16] sol–gel,[17–19] hydrothermal,[20–22] sputtering[23–25] and solution-combustion.[26,27] The *in situ* doping methods have the following advantages: (1) flexible choice of dopant materials, (2) easy control of dopant precursor concentrations, and (3) simplicity in that no additional doping steps are required. Nevertheless, *in situ* doping methods face challenges when doping NWs since dopants will inevitably affect the nucleation and anisotropic growth processes of NWs, leading to differing morphology and crystallinity or no formation of NWs.[28] On the other hand, the *ex situ* doping methods incorporate dopants as a post-processing step by methods such as ion implantation[29–31] and diffusion.[1,32] However, ion implantation is a directional doping method and it is difficult to conformally dope large aspect ratio NWs. Existing diffusion methods require special dopant precursors that limit the choice of dopant materials and frequently require capping layers that are difficult and expensive to implement on top of NWs.

Recently, we have developed a new *ex situ* sol-flame doping method, which uses high temperature flame to rapidly anneal dopant precursor coated metal oxide NWs to enable doping.[33] The high flame temperature (about 1100 °C or above) enables rapid dopant precursor decomposition and dopant diffusion into the host NWs, and also leads to high concentration of dopant incorporation. The rapid heating rate of the NWs over the flame

[a] *Department of Mechanical Engineering, Stanford University, California 94305, USA. E-mail: xlzheng@stanford.edu*
[b] *Advanced Materials Department, Jozef Stefan Institute, 1000 Ljubljana, Slovenia*
[c] *Stanford Synchrotron Radiation Lightsource, SLAC National Accelerator Laboratory, Menlo Park, California 94025, USA*
[d] *Department of Energy Resources Engineering, Stanford University, California 94305, USA*
[e] *Department of Materials Science and Engineering, Stanford University, California 94305, USA*

† Electronic supplementary information (ESI) available. See DOI: 10.1039/c4cp01748j

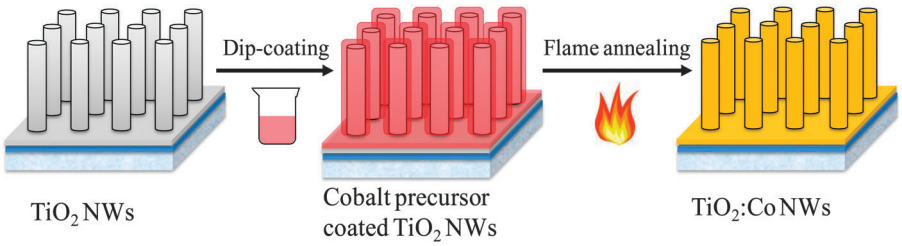

Fig. 1 Schematic of the sol-flame doping method for synthesizing TiO_2:Co NWs.

(heating up to 1100 °C in a few seconds), due to the large convective and radiative heat transfer from the burned gas in flame, minimizes the required residence time to reach the high temperature for the dopant diffusion, preventing changes in their morphology and crystallinity. The rapid cooling rate of the NWs when they are abruptly removed from the flame freezes the dopant in the lattice. The sol-flame method is a general method to dope metal oxide NWs with various different transition metals without any specific requirements on the morphology and preparation method of the NWs.[33] Further broad application of the sol-flame doping method requires the ability to control the dopant concentration and the fundamental understanding of the oxidation state and local environment of the dopant.

In this study, we select cobalt-doped TiO_2 (TiO_2:Co) NWs as a model system and investigate the influence of the cobalt (Co) concentration in the precursor solution on the Co dopant profile in TiO_2:Co NWs. We also employ various characterization methods to analyze the oxidation state and location of the Co dopant inside the TiO_2 NWs. Finally, we study the effect of Co doping concentration on the electrocatalytic activity of the TiO_2:Co NWs towards the oxygen evolution reaction (OER), which is an important reaction for electrochemical and photoelectrochemical water splitting.[34,35] We found that there is an optimal amount of Co^{2+} dopant for improving the OER activity, and our controllable sol-flame method has enabled us to study this effect. More importantly, the Co^{2+} dopants in TiO_2 NWs are more effective than the surface deposition of Co_3O_4 nanoparticles (NPs) in increasing the OER activity of TiO_2 because the Co^{2+} dopants not only have similar surface charge transfer kinetics as the Co_3O_4 NPs but also increase the bulk electrical conductivity of TiO_2.

Results and discussion

The TiO_2:Co NWs are prepared by the *ex situ* sol-flame doping method[33] as illustrated in Fig. 1. First, rutile TiO_2 NWs with an average length of 2.5 μm and diameter of 100 nm are grown on fluorine-doped tin oxide (FTO) glass substrates by the hydrothermal method[36] (see Methods section). Next, the TiO_2 NWs are dip-coated with the Co precursor solution and then air dried, leaving a uniform Co precursor film on the surface of the TiO_2 NWs. Finally, the Co precursor-coated TiO_2 NWs are annealed over a stoichiometric CH_4–air premixed flame at 1100 °C for 2 min,[37–39] which results in the decomposition of the Co precursor and rapid thermal diffusion of Co ions into the TiO_2 NW lattice, forming TiO_2:Co NWs. With this sol-flame doping method, we vary the concentration of the Co precursor solution from 0.01 M to 0.2 M to prepare a range of TiO_2:Co NW

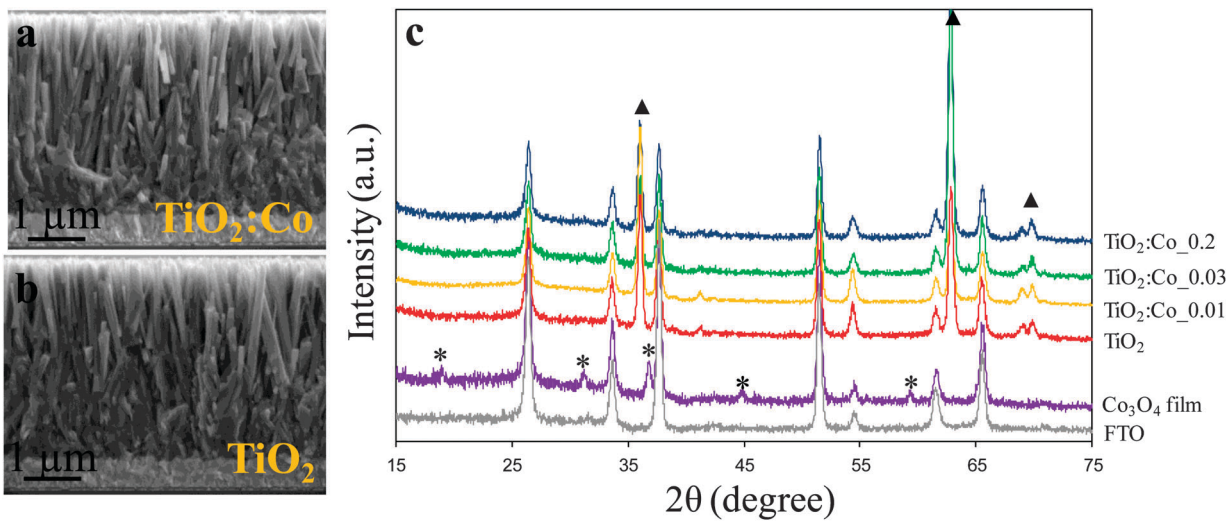

Fig. 2 Cross-sectional SEM images of (a) TiO_2:Co NWs prepared with 0.03 M Co precursor solution and (b) undoped TiO_2 NWs. (c) XRD spectra of TiO_2:Co_x (x = 0.01, 0.03 and 0.2) NWs, undoped TiO_2 NWs, reference Co_3O_4 film and FTO substrate. Symbols ▲ and * indicate peaks of rutile TiO_2 phase and cubic Co_3O_4 phase, respectively.

samples, named as TiO_2:Co_x, for which x (0.01–0.2) corresponds to the initial Co precursor concentration. Our objective is to investigate the ability of the sol-flame method to control the dopant profile.

First, we study the morphology and crystallinity of the TiO_2:Co NWs. The morphology and crystal structure of TiO_2:Co NWs are examined by scanning electron microscopy (SEM) and X-ray diffraction (XRD). The SEM images show that the TiO_2:Co NWs (Fig. 2a) have nearly identical morphology as the undoped TiO_2 NWs (Fig. 2b), demonstrating the benefit of the sol-flame method in preserving the morphology of TiO_2 NWs. The XRD spectra of the TiO_2:Co_x (x = 0.01, 0.03 and 0.2) NWs are compared with those of undoped TiO_2 NWs, a reference Co_3O_4 film sample and FTO substrate (Fig. 2c). The reference Co_3O_4 film sample is prepared by drop-casting the same 0.03 M Co precursor solution onto a FTO substrate and subsequently annealing it over the flame under identical conditions as the TiO_2:Co NWs. The reference Co_3O_4 film sample mimics the case in which the Co ions in the Co precursor shell do not diffuse into the TiO_2 NWs during flame annealing, but rather form a Co_3O_4 film on the NW surface. The XRD patterns in Fig. 2c clearly show that the three TiO_2:Co_x (x = 0.01, 0.03 and 0.2) NW samples have peaks that are identical to those of the undoped rutile TiO_2 NWs and have no peaks that overlap with those of the reference Co_3O_4 film sample. These results suggest that the sol-flame method neither modifies the crystallinity of the TiO_2 NWs nor forms detectable amounts of crystalline Co_3O_4 particles or films on the TiO_2 NW surface.

The surface and the lattice spacing of the TiO_2:Co NWs are further examined in detail by transmission electron microscopy (TEM). The low magnification TEM images show that all the TiO_2:Co_x NWs (x = 0.01–0.2) (Fig. 3b–e) have similar shape as the undoped TiO_2 NW (Fig. 3a). The high resolution TEM images show that all the TiO_2:Co_x NWs (x = 0.01–0.2) (Fig. 3b–e) are crystalline with the same lattice spacing as the undoped rutile TiO_2 NW (Fig. 3a), implying that the Co dopants do not significantly distort the lattice of TiO_2 due to the similar radius of Co ion and Ti ion.[40] However, TiO_2:Co NWs with different Co precursor concentrations exhibit different surface characteristics. For low Co precursor concentration, the surfaces of TiO_2:Co_0.01 NW (Fig. 3b), TiO_2:Co_0.03 NW (Fig. 3c) and TiO_2:Co_0.05 NW (Fig. 3d) are relatively smooth and similar to the undoped TiO_2 NW (Fig. 3a). With high Co precursor concentration, the surface of TiO_2:Co_0.2 NW (Fig. 3e) is sparsely decorated with small NPs of 5 nm in diameter or less, and the electron diffraction pattern of these NPs (Fig. 3k) shows that they are cubic Co_3O_4. The formation of surface Co_3O_4 NPs can be ascribed to the saturation of Co dopants in the bulk of

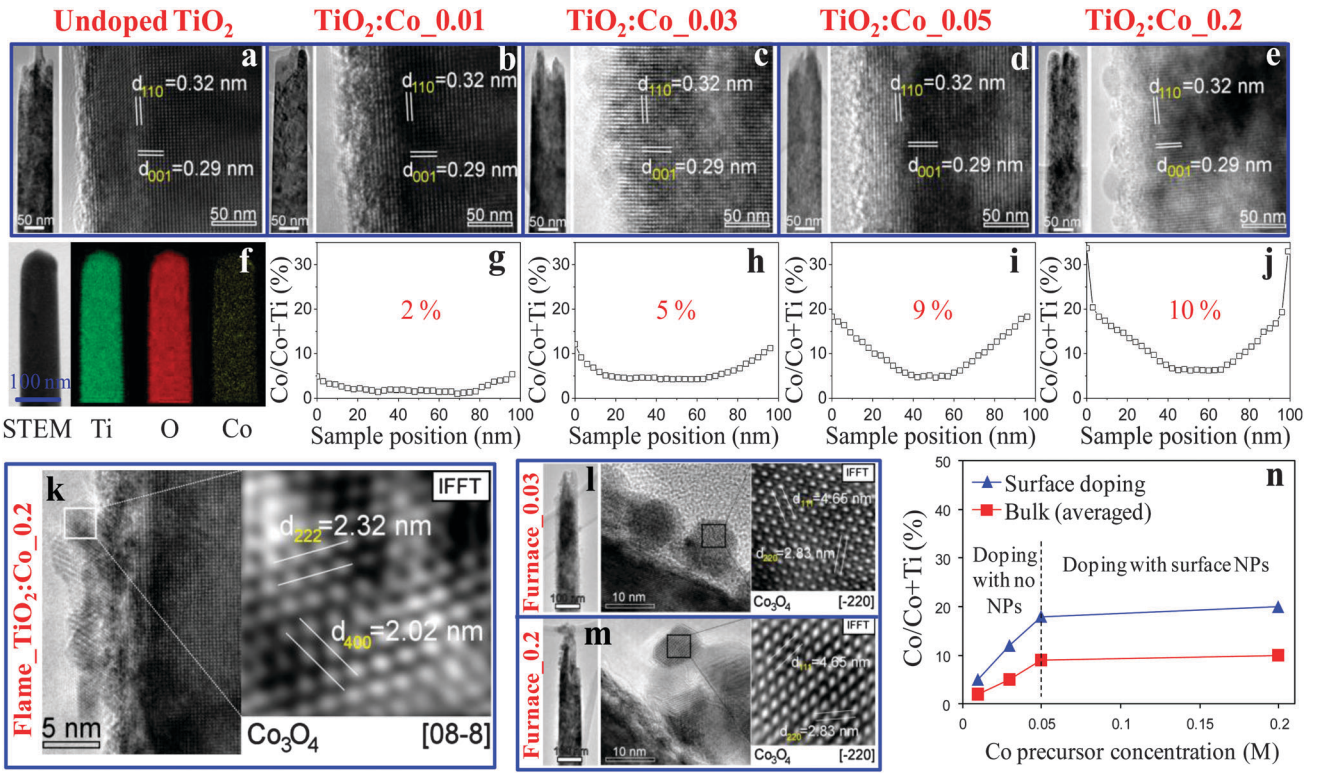

Fig. 3 TEM images of (a) undoped TiO_2, (b) TiO_2:Co_0.01, (c) TiO_2:Co_0.03, (d) TiO_2:Co_0.05 and (e) TiO_2:Co_0.2 NWs (left: low magnification TEM image of single NW, right: high resolution TEM image of the NW edge with corresponding crystal lattice parameters). (f) EDS mapping of elements Ti, O and Co in TiO_2:Co_0.03 NW. Radial doping profiles for Co in (g) TiO_2:Co_0.01, (h) TiO_2:Co_0.03, (i) TiO_2:Co_0.05 and (j) TiO_2:Co_0.2 NW obtained by point-by-point EELS analysis (the percentage values represent the averaged doping concentration of Co in the bulk). TEM images and electron diffraction patterns of the NPs on the surface of (k) flame-annealed TiO_2:Co_0.2 NWs, (l) furnace-annealed TiO_2 NWs that are dip-coated with 0.03 M Co precursor solution and (m) furnace-annealed TiO_2 NWs that are dip-coated with 0.2 M Co precursor solution. (n) Plot of the Co dopant concentrations on the surface and averaged in the bulk *versus* the Co precursor concentration.

TiO_2 NWs and the precipitation of excess cobalt on the NW surface. Finally, to illustrate the advantages of flame annealing for doping NWs, we also annealed the same Co precursor-coated TiO_2 NWs at low temperature (350 °C) in a furnace for 1 h. In comparison, with low temperature and long time furnace annealing, the Co precursor, regardless of their concentrations, does not diffuse into the TiO_2 lattice, but rather forms Co_3O_4 NPs of 10 nm in diameter or larger on the TiO_2 NW surface (Fig. 3l and m). This comparison between the flame annealing (Fig. 3c and e) and furnace annealing (Fig. 3l and m) clearly illustrates that the high flame temperature (1100 °C for 2 minutes) effectively enables the rapid dopant precursor decomposition and dopant diffusion into the host NWs.

Next, we investigate the controllability of the Co dopant profile. The Co dopant spatial distribution along the TiO_2:Co NW diameter is measured by energy dispersive spectroscopy (EDS) mapping and electron energy loss spectroscopy (EELS) spectra. The EDS elemental mapping analysis (Fig. 3f) of TiO_2:Co NW clearly shows that Co is doped over the entire TiO_2 NW. The EELS measurements show that the radial doping profiles of Co dopant in all the TiO_2:Co NWs have a Gaussian-like shape with higher Co concentration on the surface (Fig. 3g–j), indicating that the Co distribution is caused by a radial thermal diffusion process. In addition, the surface and overall Co dopant concentrations clearly increase with increasing the Co precursor concentration (Fig. 3n), which demonstrates that the doping profile can be readily controlled through the concentration of the dopant precursor solution with our sol-flame doping method. For TiO_2:Co_0.2 NW (Fig. 3j), the Co dopant concentration abruptly decreases from 35 at% to 20 at% within the top 5 nm of the NW surface and then gradually decreases along the radial direction of the NW. The sharp dopant concentration change near the top 5 nm surface is consistent with the observed additional Co_3O_4 NP formation on the NW surface for high Co precursor concentration as shown in the TEM image in Fig. 3e. The Co concentration of 20 at% in the sub-layer beneath the precipitates of TiO_2:Co_0.2 NW (Fig. 3j) is about the same as the 18 at% Co on the surface of TiO_2:Co_0.05 NW (Fig. 3i), which suggests that the doping limit of Co dopant is about 18–20 at% in the TiO_2 NW *via* the sol-flame method. The doping limit of 18–20 at% is considerably higher than the previously reported doping limit of about 12 at% for TiO_2:Co by other doping methods.[41–43] The higher doping limit by the sol-flame method is due to the high temperature of flame and the rapid cooling rate ($\sim$800 K min^{-1}) caused by abrupt removal of NWs from the flame, which quenches the diffusion of dopants in the host TiO_2 lattice and prevents them from precipitation during the cooling process.

Then, we analyze the oxidation states and local environment of the Co dopant in the TiO_2 NWs. The oxidation states of Co near the surface of TiO_2:Co NWs are characterized by X-ray photoelectron spectroscopy (XPS). As shown in Fig. 4a, the Co $2p_{3/2}$ peak positions for TiO_2:Co_0.2 NWs and TiO_2:Co_0.03 NWs are at 780.1 and 779.7 eV, respectively, which are 0.6 and 0.2 eV higher than that of 779.5 eV for the reference Co_3O_4 film (the same one used for XRD shown in Fig. 2c). Similar up-shifting is also observed for the Co $2p_{1/2}$ peak positions and the amount

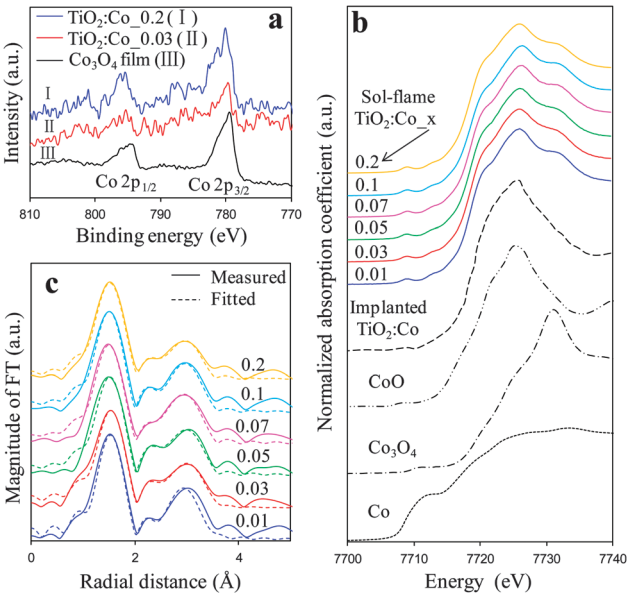

Fig. 4 (a) Co 2p XPS spectra of TiO_2:Co_0.03, TiO_2:Co_0.2 and Co_3O_4 film. (b) Co K-edge XANES spectra for TiO_2:Co_x (x = 0.01–0.2) NWs by sol-flame, Co metal, Co_3O_4, CoO taken from ref. 46 and ion-implanted rutile TiO_2:Co taken from ref. 47. (c) Measured and fitted radial distribution functions for Co K-edge EXAFS data from TiO_2:Co_x (x = 0.01–0.2) NWs.

of peak energy shift increases with increasing Co dopant concentration. It should be noted that the Co_3O_4 NPs only slightly cover the surface of TiO_2:Co_0.2 NWs as revealed by the TEM (Fig. 3e), so most of the XPS signal comes from the doped Co near the top 10 nm layer of the TiO_2:Co NWs. The shifting of both Co $2p_{3/2}$ and $2p_{1/2}$ peaks towards higher binding energy reveals that the chemical state of Co near the surface of TiO_2:Co NWs is different from that of reference Co_3O_4 film, and the Co 2p peak positions for TiO_2:Co_0.2 NWs actually match with those for CoO reported by ref. 44 and 45. Hence, the XPS analysis suggests that the oxidation state of the Co dopant near the surface of TiO_2:Co NWs is primarily 2+ with possible small amount of 3+. To further understand the oxidation states of Co dopants in the entire volume of the TiO_2:Co NWs, the Co K-edge X-ray absorption near edge structure (XANES) spectra are measured for the TiO_2:Co_x (x = 0.01–0.2) NWs and further compared with the spectra of various Co-containing reference materials, including Co metal, Co_3O_4, CoO[46] and ion-implanted Co-doped rutile TiO_2 (110) (Implanted_TiO_2:Co, for which the oxidation state of Co was reported to be 2+)[47] (Fig. 4b). Both the XANES spectral shape and edge position of the TiO_2:Co_x (x = 0.01–0.2) NWs are significantly different from those of Co and Co_3O_4, but they resemble those of the ion-implanted TiO_2:Co and CoO references, which supports the XPS analysis in that the oxidation state of the Co dopant in the TiO_2:Co NWs is primarily 2+. The local environment of the Co dopant is further studied by analyzing the Co K-edge extended X-ray absorption fine structure (EXAFS) for the TiO_2:Co_x (x = 0.01–0.2) NWs (Fig. 4c). The experimentally measured Co K-edge EXAFS data are fitted by assuming that Co substitutes the Ti site in the rutile TiO_2 model in which each Ti is surrounded by six O atoms with two

distinct bond lengths in the first shell and two Ti atoms in the second shell. The peak modeled from the scattering by the first O shell fits well to the first peak of the measured Fourier transformed (FT) EXAFS data. However, the second peak of the measured FT-EXAFS data cannot be fitted well by the assumption of two Ti atoms in the second shell. Inclusion of additional Ti atoms in the second shell greatly improves the quality of the fit (Fig. 4c). These additional Ti atoms in the second shell probably come from the Co-substituted Ti atoms that are now occupying the interstitial sites. In addition, the structural parameters extracted from the fitting (Table S1, ESI†) show that the total number of O coordinated to Co in the first shell is smaller than six for the TiO_2:Co NWs, suggesting that there are some oxygen vacancies near the Co dopants. EELS measurement was further conducted to verify the existence of oxygen vacancies in the TiO_2:Co NWs (Table S2, ESI†). The O/(Ti + Co) ratios measured by EELS for TiO_2:Co_0.03 and TiO_2:Co_0.2 NWs are 1.97 and 1.88, respectively, corresponding to 1.5% and 6% oxygen vacancies. Hence, we conclude that the Co ions are substitutionally doped into the octahedral Ti sites in the rutile TiO_2 lattice, and the Co ions push the Co-substituted Ti into the interstitial sites and generate small amount of oxygen vacancies near the Co dopants.

The effect of Co doping on the electrocatalytic activity of TiO_2 NWs for the OER is investigated using the cyclic voltammetry (CV) measurement. Fig. 5a shows the anodic-going sweep of typical CV cycles for TiO_2:Co_x (x = 0.01–0.2) and undoped TiO_2 NWs. Compared to undoped TiO_2 NWs, all the TiO_2:Co NWs show significantly enhanced OER activity as evidenced by the much higher current density at a given potential in the range of 1.8 to 3 V *vs.* RHE. The overpotentials for undoped TiO_2 and different TiO_2:Co NWs to reach current density of 0.1 mA cm^{-2} are further compared in Fig. 5b. All the TiO_2:Co NWs exhibit lower overpotentials than the undoped TiO_2 NWs. The similar overpotential for TiO_2:Co_x ($x > 0.05$) NWs is probably due to the fact they have very similar dopant concentration distribution (~10 at% in the bulk and 20 at% on the surface) and similar impurity phase (Co_3O_4 NPs) on the surface. The lowest overpotential of 0.72 V (highest OER activity) is achieved by the TiO_2:Co_0.03 NWs (12 at% of Co on the surface), which is 0.76 V lower than the overpotential of 1.48 V for undoped TiO_2 NWs. To gain more insight on the enhanced OER activity of TiO_2 by Co doping, Tafel plots are plotted in Fig. 5c. The exchange current densities of TiO_2:Co NWs, determined as the extrapolated x-intercept of the Tafel plot, are about 1–3 orders of magnitude higher than that of the undoped TiO_2 NWs, suggesting that TiO_2:Co NWs have much more facile charge transfer kinetics on the surface than undoped TiO_2 NWs.[48–51] The observed higher exchange current densities of TiO_2:Co NWs cannot be attributed to the change in the surface area, since the specific surface areas of the undoped TiO_2 and TiO_2:Co NWs measured by the Brunauer–Emmett–Teller (BET) method using nitrogen as probe gas are in the same order of magnitude (Table S3, ESI†). Instead, the increased surface activity towards the OER by substitutional doping of transition metals on the surface of TiO_2, according to the theoretical density functional theory calculations, comes from the surface states and surface resonance states localized on the dopants that enhance the binding strength between the intermediate adsorbates and the doped TiO_2 surface.[52,53] On the other hand, doping also modifies the electrical conductivity of TiO_2, which strongly affects the overpotential

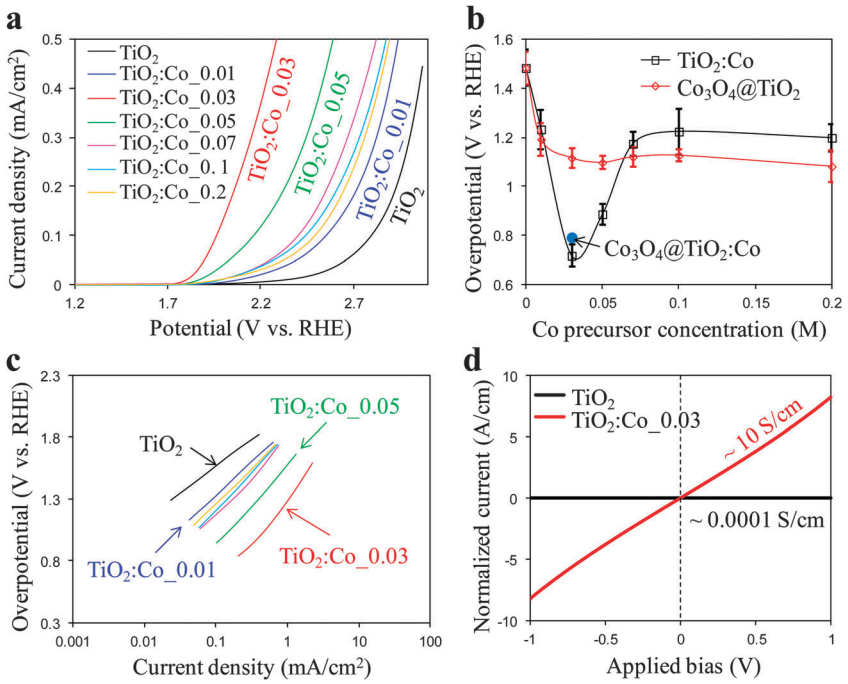

Fig. 5 (a) The anodic-going sweep of typical cyclic voltammograms for TiO_2:Co_x (x = 0.01–0.2) and undoped TiO_2 NWs. (b) Plot of overpotentials of TiO_2:Co, Co_3O_4@TiO_2 and Co_3O_4@TiO_2:Co NWs at current density of 0.1 mA cm^{-2} *versus* the concentration of cobalt precursor solution. (c) Tafel plots of TiO_2:Co_x (x = 0.01–0.2) and undoped TiO_2 NWs. (d) Current–voltage curves of single TiO_2:Co_0.03 NW and undoped TiO_2 NW.

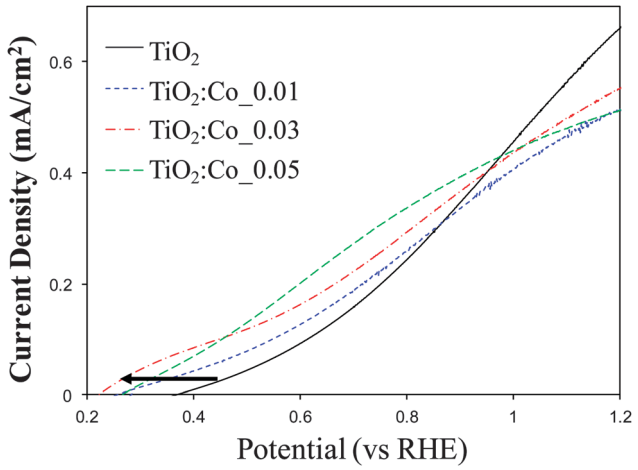

Fig. 6 Photocurrent density–potential (*J*–*V*) curves of undoped TiO_2 and TiO_2:Co_*x* (*x* = 0.01–0.05) NWs.

for the OER. The conductivity measurement of a single NW clearly shows that Co doping increases the conductivity of TiO_2 NWs by about five orders of magnitude (Fig. 5d). Hence, doping TiO_2 NWs with Co improves both surface charge transfer kinetics and bulk electrical conductivity, leading to enhanced OER activity for TiO_2:Co NWs. Finally, when the TiO_2:Co NWs are used as photoanodes for the photoelectrochemical (PEC) water splitting system, the onset potential shows a cathodic shift of 100–150 mV (Fig. 6).

The OER activity of the TiO_2:Co NWs are further compared with the as-grown TiO_2 NWs that are decorated with Co_3O_4 NP electrocatalysts on the surface (Co_3O_4@TiO_2), and such comparison is aimed to differentiate and compare the roles of Co^{2+} dopant and Co_3O_4 surface catalyst on affecting the OER activity. The control Co_3O_4@TiO_2 NWs were prepared by annealing Co precursor-coated TiO_2 NWs at low temperature (350 °C) in a furnace for 1 h. As shown in Fig. 5b, the Co_3O_4@TiO_2 NWs exhibit larger overpotential than the optimal TiO_2:Co_0.03 NWs, which suggests that the Co^{2+} dopants are more effective than Co_3O_4 NPs in enhancing the OER activity. In addition, when we further decorated the optimal TiO_2:Co_0.03 NWs with additional Co_3O_4 NPs (noted as Co_3O_4@TiO_2:Co), it does not change the overpotential for OER (Fig. 5b). Since the only difference between TiO_2:Co_0.03 and Co_3O_4@TiO_2:Co is their surface composition, it indicates that the TiO_2:Co surface has similar surface charge transfer kinetics as the Co_3O_4 NPs. Hence, the better OER activity observed for the TiO_2:Co_0.03 NWs (doping), in comparison to Co_3O_4 NPs decorated TiO_2 NWs (surface modification only), comes from the conductivity improvement by doping.

Conclusions

In summary, we present a controllable and reliable sol-flame doping method for the synthesis of TiO_2:Co NWs that exhibit significantly enhanced electrocatalytic activity for the OER as compared to undoped TiO_2 NWs. The sol-flame doping method allows fine control over the Co dopant profile by varying the concentration of Co precursor solution while preserving the morphology and crystallinity of host TiO_2 NWs. Characterizations of the TiO_2:Co NWs show that Co dopants exhibit 2+ oxidation state and substitutionally occupy the Ti sites in the TiO_2 lattice. The TiO_2:Co NWs exhibit enhanced and dopant concentration dependent OER activity and PEC performance. The TiO_2:Co NWs with 12 at% of Co on the surface (averaged 5 at% in the bulk) shows the highest electrocatalytic activity for the OER, which reduces the overpotential by 760 mV with respect to the undoped TiO_2 NWs. The TiO_2:Co NWs also exhibit a cathodic shift of about 100–150 mV for the onset potential when used as photoanodes for the PEC water-splitting system. The significant OER overpotential reduction and cathodic shift of the onset potential for TiO_2:Co NWs come from two factors: (1) the Co^{2+} dopant improves the surface charge transfer kinetics and is as effective as the Co_3O_4 NPs; and (2) the Co^{2+} dopant also significantly increases the bulk electrical conductivity of TiO_2. With the demonstrated controllability, we believe that the sol-flame doping method will be a general and promising technique for effective doping of diverse nanostructured materials.

Methods

Synthesis of rutile TiO_2 NW arrays

The rutile TiO_2 NW arrays were synthesized on TiO_2 seed layer coated FTO (fluorine-doped tin oxide) substrates using the hydrothermal method, the details of which were reported in our previous work.[33,36] Briefly for a typical synthesis, 0.6 mL of titanium(IV) butoxide (Aldrich Chemicals, 97%) was added into 50 mL of an aqueous HCl solution (25 mL of deionized (DI) water + 25 mL of concentrated HCl (38%)) under magnetic stirring. After stirring for 5 min, the solution was poured into a Teflon-lined stainless steel autoclave (100 mL capacity) and pieces of the TiO_2 seed layer coated FTO substrates, which have been cleaned for 10 min using an ultrasonicator in a mixed solution of DI water, acetone and iso-propanol, were immersed in the solution. The autoclave was sealed and heated to 170 °C in an oven, held at 170 °C for 6 h and then cooled to room temperature naturally. The obtained samples were washed with DI water and finally annealed at 450 °C for 1 h in air.

Preparation of cobalt precursor solution

The cobalt precursor solutions were prepared by dissolving cobalt acetate tetrahydrate ($Co(CH_3COO)_2{\cdot}4H_2O$, 99%, Sigma-Aldrich Chemicals) into 10 mL 2-methoxyethanol ($C_3H_8O_2$, >99%, Acros Organics) and followed by sonication for 30 min. The concentration of cobalt acetate tetrahydrate was varied between 0.01–0.2 M.

Dip-coating

The TiO_2 NWs on FTO substrates were vertically dipped into the Co precursor solution, kept in the solution for 15 s and then withdrawn vertically at a constant speed of 1 mm s^{-1}. Finally, the coated TiO_2 NWs were dried in air to remove excess solvent.

Flame annealing

The flame annealing was conducted using a 6 cm diameter co-flow premixed flat flame burner (McKenna Burner) which operates on premixed CH_4 (fuel) and air (oxidizer).[37–39] The flow rates of CH_4 and air were 2.05 and 19.52 SLPM, respectively, yielding an overall fuel/oxygen equivalence ratio of $\Phi = 1$. The Co precursor-coated TiO_2 NW sample was inserted into the post-flame region at a height of 2.5 cm above the flame front. After 2 min annealing, the sample was abruptly removed from the post-flame region and cooled to room temperature in ambient environment. The flame annealing temperature was measured to be about 1100 °C by a K-type thermocouple (1/16 in. bead size, Omega Engineering, Inc.).

Material characterization

The morphologies of doped and undoped TiO_2 NWs were examined using scanning electron microscopy (SEM, FEI Sirion XL30, 5 kV) and transmission electron microscopy (TEM, FEI Tecnai G2 F20 X-TWIN FEG, 200 kV). The phase and crystallinity were examined using parallel beam X-ray diffraction (XRD, PANalytical XPert 2, 45 kV, 40 mA). The dopant distribution and concentration were examined using an energy dispersive X-ray spectrometer (EDS) and an electron energy loss spectrometer (EELS) equipped in the TEM. The EELS spectra were collected with an energy resolution of 1.0 ± 0.2 eV at a dispersion of 0.5 eV per channel, a convergence semi-angle of 9.6 mrad and collection semi-angle of 24. The spectra were acquired across the NW diameter using a line profile feature in Tecnai imaging and Analysis (TIA) software. During the experiment, the incident electron beam was perpendicular to the TiO_2 NW. A new spectrum was collected every 3 nm. EELs data were post processed in Digital micrograph. The background of the spectra was subtracted using the Power-law model. The spectrum processing for elemental quantification was performed with Digital Micrograph EELS analysis. The quantification of the Co dopant element in the TiO_2 NW was carried out *via* Hartree–Slater for Co and Ti edges. The chemical state of the Co dopant was examined by X-ray photoelectron spectroscopy (XPS, SSI S-Probe, Al-Kα, 1486 eV, 150×800 μm spot) with binding energies referenced to adventitious carbon at 284.6 eV. The local environment of Co dopant was examined by X-ray adsorption spectroscopy (XAS) collected using the fluorescence mode on beamline 11-2 at Stanford Synchrotron Radiation Lightsource (SSRL). Fitting of EXAFS data was performed using SIXPACK and FEFF analysis software.

Electrochemical and photoelectrochemical (PEC) characterization

The electrochemical and PEC measurements were carried out using a potentiostat (Model SP-200, BioLogic) in a three-electrode compression cell. The TiO_2:Co NWs or undoped TiO_2 NWs supported on FTO glass substrate served as the working electrode with a saturated calomel reference electrode (SCE) and a Pt wire counter electrode. 1 M KOH under continuous Ar purging was used as the electrolyte. For the measurement of the cyclic voltammograms of the OER activity, the voltage was swept linearly from -1.0 to 2.0 V_{SCE} at a scan rate of 20 mV s^{-1}. For the evaluation of the PEC performance, the photocurrent–potential (J–V) curves were measured under simulated solar light illumination (AM1.5G, 100 mW cm^{-2}) at a scan rate of 50 mV s^{-1} from -1.0 to 2.0 V_{SCE}.

Electrical conductivity measurement

The NWs were sonicated in IPA and then drop-cast onto a SiO_2/Si substrate. Platinum (Pt) metal contacts were deposited on two ends of each TiO_2 NWs using the focused-ion beam (FIB, FEI Strata DB235). Current–voltage (I–V) measurements were conducted at room temperature using a semiconductor analyzer (Model 4200-SCS, Keithley) with tungsten probes.

Surface area measurement

The nitrogen sorption analysis of undoped TiO_2 and TiO_2:Co NWs (mechanically scratched off from the FTO substrate) was performed using 99.999% pure nitrogen gas at 77 K in an Autosorb iQ_2 low-pressure gas sorption analyzer (Quantachrome). The samples were outgassed at 0.03 Torr and 200 °C for 12 hours prior to measurements. The specific surface areas were obtained by the Brunauer–Emmett–Teller (BET) method based upon the adsorption data in the partial pressure (p/p_0) range of 0.05 to 0.2.

Acknowledgements

This material is based upon work supported by the Center on Nanostructuring for Efficient Energy Conversion, an Energy Frontier Research Center funded by the U.S. Department of Energy, Office of Science, Office of Basic Energy Sciences under Award Number DE-SC0001060.

References

1 J. C. Ho, R. Yerushalmi, Z. A. Jacobson, Z. Fan, R. L. Alley and A. Javey, *Nat. Mater.*, 2008, **7**, 62–67.
2 Z. Teukam, J. Chevallier, C. Saguy, R. Kalish, D. Ballutaud, M. Barbe, F. Jomard, A. Tromson-Carli, C. Cytermann, J. E. Butler, M. Bernard, C. Baron and A. Deneuville, *Nat. Mater.*, 2003, **2**, 482–486.
3 J. Ristein, *Science*, 2006, **313**, 1057–1058.
4 Y. Gassenbauer and A. Klein, *J. Phys. Chem. B*, 2006, **110**, 4793–4801.
5 X. Wang, J. A. Rodriguez, J. C. Hanson, D. Gamarra, A. Martínez-Arias and M. Fernández-García, *J. Phys. Chem. B*, 2005, **109**, 19595–19603.
6 R. T. Wegh, H. Donker, K. D. Oskam and A. Meijerink, *Science*, 1999, **283**, 663–666.
7 S. S. Iyer and Y. H. Xie, *Science*, 1993, **260**, 40–46.
8 Y. Matsumoto, M. Murakami, T. Shono, T. Hasegawa, T. Fukumura, M. Kawasaki, P. Ahmet, T. Chikyow, S.-y. Koshihara and H. Koinuma, *Science*, 2001, **291**, 854–856.
9 J. M. D. Coey, M. Venkatesan and C. B. Fitzgerald, *Nat. Mater.*, 2005, **4**, 173–179.

10 P. Sharma, A. Gupta, K. V. Rao, F. J. Owens, R. Sharma, R. Ahuja, J. M. O. Guillen, B. Johansson and G. A. Gehring, *Nat. Mater.*, 2003, **2**, 673–677.
11 Y. Cui, Q. Q. Wei, H. K. Park and C. M. Lieber, *Science*, 2001, **293**, 1289–1292.
12 X. F. Duan, Y. Huang, Y. Cui, J. F. Wang and C. M. Lieber, *Nature*, 2001, **409**, 66–69.
13 J. Wallentin, N. Anttu, D. Asoli, M. Huffman, I. Aberg, M. H. Magnusson, G. Siefer, P. Fuss-Kailuweit, F. Dimroth, B. Witzigmann, H. Q. Xu, L. Samuelson, K. Deppert and M. T. Borgstrom, *Science*, 2013, **339**, 1057–1060.
14 R. Franking, L. Li, M. A. Lukowski, F. Meng, Y. Tan, R. J. Hamers and S. Jin, *Energy Environ. Sci.*, 2013, **6**, 500–512.
15 S. J. Han, T. H. Jang, Y. B. Kim, B. G. Park, J. H. Park and Y. H. Jeong, *Appl. Phys. Lett.*, 2003, **83**, 920–922.
16 F. D. Morrison, D. C. Sinclair and A. R. West, *J. Appl. Phys.*, 1999, **86**, 6355–6366.
17 D. Levy and L. Esquivias, *Adv. Mater.*, 1995, **7**, 120–129.
18 K. Binnemans, *Chem. Rev.*, 2009, **109**, 4283–4374.
19 N. Uekawa and K. Kaneko, *Adv. Mater.*, 1995, **7**, 312–315.
20 X. Zhou, F. Peng, H. Wang and H. Yu, *J. Solid State Chem.*, 2011, **184**, 3002–3007.
21 K. Riwotzki and M. Haase, *J. Phys. Chem. B*, 1998, **102**, 10129–10135.
22 R. X. Yan and Y. D. Li, *Adv. Funct. Mater.*, 2005, **15**, 763–770.
23 T. Lindgren, J. M. Mwabora, E. Avendano, J. Jonsson, A. Hoel, C. G. Granqvist and S. E. Lindquist, *J. Phys. Chem. B*, 2003, **107**, 5709–5716.
24 J. Wang, Z. Gu, M. H. Lu, D. Wu, C. S. Yuan, S. T. Zhang, Y. F. Chen, S. N. Zhu and Y. Y. Zhu, *Appl. Phys. Lett.*, 2006, **88**, 252110.
25 J. G. Lu, S. Fujita, T. Kawaharamura, H. Nishinaka, Y. Kamada, T. Ohshima, Z. Z. Ye, Y. J. Zeng, Y. Z. Zhang, L. P. Zhu, H. P. He and B. H. Zhao, *J. Appl. Phys.*, 2007, **101**, 083705.
26 S. S. Thind, G. Wu and A. Chen, *Appl. Catal., B*, 2012, **111–112**, 38–45.
27 K. Nagaveni, M. S. Hegde and G. Madras, *J. Phys. Chem. B*, 2004, **108**, 20204–20212.
28 J. Wallentin and M. T. Borgstrom, *J. Mater. Res.*, 2011, **26**, 2142–2156.
29 L. N. Large and R. W. Bicknell, *J. Mater. Sci.*, 1967, **2**, 589–609.
30 A. Ghicov, J. M. Macak, H. Tsuchiya, J. Kunze, V. Haeublein, L. Frey and P. Schmuki, *Nano Lett.*, 2006, **6**, 1080–1082.
31 T. Burchhart, C. Zeiner, A. Lugstein, C. Henkel and E. Bertagnolli, *Nanotechnology*, 2011, **22**, 035201.
32 K. E. Moselund, H. Ghoneim, H. Schmid, M. T. Björk, E. Lörtscher, S. Karg, G. Signorello, D. Webb, M. Tschudy, R. Beyeler and H. Riel, *Nanotechnology*, 2010, **21**, 435202.
33 I. S. Cho, C. H. Lee, Y. Feng, M. Logar, P. M. Rao, L. Cai, D. R. Kim, R. Sinclair and X. Zheng, *Nat. Commun.*, 2013, **4**, 1723.
34 T. R. Cook, D. K. Dogutan, S. Y. Reece, Y. Surendranath, T. S. Teets and D. G. Nocera, *Chem. Rev.*, 2010, **110**, 6474–6502.
35 M. G. Walter, E. L. Warren, J. R. McKone, S. W. Boettcher, Q. Mi, E. A. Santori and N. S. Lewis, *Chem. Rev.*, 2010, **110**, 6446–6473.
36 I. S. Cho, Z. Chen, A. J. Forman, D. R. Kim, P. M. Rao, T. F. Jaramillo and X. Zheng, *Nano Lett.*, 2011, **11**, 4978–4984.
37 Y. Feng, I. S. Cho, P. M. Rao, L. Cai and X. Zheng, *Nano Lett.*, 2013, **13**, 855–860.
38 L. Cai, P. M. Rao, Y. Feng and X. Zheng, *Proc. Combust. Inst.*, 2013, **34**, 2229–2236.
39 Y. Feng, I. S. Cho, L. Cai, P. M. Rao and X. Zheng, *Proc. Combust. Inst.*, 2013, **34**, 2179–2186.
40 R. Shannon, *Acta Crystallogr., Sect. A: Cryst. Phys., Diffr., Theor. Gen. Crystallogr.*, 1976, **32**, 751–767.
41 J. Rebecca, G. Priya and A. S. Nicola, *J. Phys.: Condens. Matter*, 2005, **17**, R657.
42 N. H. Hong, J. Sakai, W. Prellier and A. Hassini, *Appl. Phys. Lett.*, 2003, **83**, 3129–3131.
43 W. K. Park, R. J. Ortega-Hertogs, J. S. Moodera, A. Punnoose and M. S. Seehra, *J. Appl. Phys.*, 2002, **91**, 8093–8095.
44 M. C. Biesinger, B. P. Payne, A. P. Grosvenor, L. W. M. Lau, A. R. Gerson and R. S. C. Smart, *Appl. Surf. Sci.*, 2011, **257**, 2717–2730.
45 N. S. McIntyre, D. D. Johnston, L. L. Coatsworth, R. D. Davidson and J. R. Brown, *Surf. Interface Anal.*, 1990, **15**, 265–272.
46 G. Jacobs, Y. Y. Ji, B. H. Davis, D. Cronauer, A. J. Kropf and C. L. Marshall, *Appl. Catal., A*, 2007, **333**, 177–191.
47 V. Shutthanandan, S. Thevuthasan, S. M. Heald, T. Droubay, M. H. Engelhard, T. C. Kaspar, D. E. McCready, L. Saraf, S. A. Chambers, B. S. Mun, N. Hamdan, P. Nachimuthu, B. Taylor, R. P. Sears and B. Sinkovic, *Appl. Phys. Lett.*, 2004, **84**, 4466–4468.
48 N. S. Lewis, *J. Phys. Chem. B*, 1998, **102**, 4843–4855.
49 S. K. Haram, in *Handbook of Electrochemistry*, ed. G. Z. Cynthia, Elsevier, Amsterdam, 2007, pp. 329–389.
50 R. A. Marcus, *J. Chem. Phys.*, 1956, **24**, 966–978.
51 A. J. Bard and L. R. Faulkner, *Electrochemical Methods: Fundamentals and Applications*, Wiley, 2000.
52 M. García-Mota, A. Vojvodic, H. Metiu, I. C. Man, H.-Y. Su, J. Rossmeisl and J. K. Nørskov, *ChemCatChem*, 2011, **3**, 1607–1611.
53 M. García-Mota, A. Vojvodic, F. Abild-Pedersen and J. K. Nørskov, *J. Phys. Chem. C*, 2012, **117**, 460–465.

